Computers and Structures 330 (2026) 108356

Contents lists available at ScienceDirect

Computers and Structures

journal homepage: www.elsevier.com/locate/cas

# Finite-strain identification of hyperelastic polyurethane adhesive using the virtual fields method

Marcin Nowak [a,*], Paweł Szeptyński [c], Sandra Musiał [b], Klaudia Śliwa-Wieczorek [d], Michał Maj [b]

[a] Institute of Structural Analysis, Faculty of Civil and Transport Engineering, Poznan University of Technology, ul. Jacka Rychlewskiego 1, 61-131 Poznań, Poland
[b] Institute of Fundamental Technological Research, Polish Academy of Sciences, Pawińskiego 5B, 02-106 Warsaw, Poland
[c] Chair of Structural Mechanics and Material Mechanics, Faculty of Civil Engineering, Cracow University of Technology, ul. Warszawska 24, 31-155 Kraków, Poland
[d] Chair of Bridge, Metal and Timber Structures, Faculty of Civil Engineering, Cracow University of Technology, ul. Warszawska 24, 31-155 Kraków, Poland

ARTICLE INFO

*Keywords:*
Identification of material constants
Digital image correlation
Finite element analysis
Optimization
Hyperelasticity
Compliant adhesives

ABSTRACT

A finite-strain identification framework based on the Virtual Fields Method (VFM) is proposed for the characterization of hyperelastic polymer materials subjected to heterogeneous deformation. The approach exploits full-field displacement measurements obtained by digital image correlation during physical experiments and formulates the inverse problem through the principle of virtual work. To enhance parameter sensitivity and identifiability, a T-shaped specimen together with a dedicated experimental setup was specifically designed to generate pronounced nonuniform strain fields from the onset of loading. The constitutive response is described within a finite deformation setting using hyperelastic strain-energy density functions, and the unknown material parameters are determined by direct inversion of the weak form of the equilibrium equations. A dedicated integration strategy based on Voronoi tessellation of the measurement points is developed to ensure consistent evaluation of the virtual work integrals. The proposed framework is assessed using both experimental data and synthetic data generated by nonlinear finite element simulations. The results demonstrate accurate and robust recovery of hyperelastic parameters, highlighting the effectiveness of the combined experimental–numerical approach and specimen design with an enhanced VFM formulation for reliable material characterization at finite strains.

## 1. Introduction

The reliable identification of material properties is essential for the design and analysis of engineering structures. Accurate knowledge of constitutive behavior allows for better prediction of performance and ensures safety across a wide range of applications. Conventional identification methods based on recorded force-displacement dependencies often face challenges when dealing with complex loading conditions or advanced materials. Consequently, the search for improved strategies to characterize materials has become a central topic in experimental mechanics. One of the effective approaches for material identification is the Virtual Fields Method (VFM) [1], which utilizes the principle of virtual work. By applying VFM, the material parameters can be obtained directly from experimental data, even under complex loading conditions. This method is particularly advantageous for polymers, the mechanical properties of which often exhibit nonlinearity and time-dependency. Through VFM, it is possible to obtain accurate and reliable constitutive parameters [2], which are essential in various engineering and industrial domains. The VFM has emerged as a powerful tool in this context, enabling the determination of material constants by the use of full-field strain and displacement data. These data are often obtained through techniques like Digital Image Correlation (DIC) [3], which provide detailed deformation fields during mechanical testing. VFM's utility lies in its ability to integrate full-field measurement techniques with innovative testing setups. It is particularly effective in analyzing hyperelastic models, such as the Mooney and Ogden models ([4,5]) which describe the nonlinear stress-strain behavior characteristic.

In addition to the static characterization of the materials, VFM has proven essential in assessing the dynamic and relaxation behaviors of hyperelastic materials [2,6]. By utilizing strain-rate dependent and dynamic loading data, the method has been used to analyze viscoelastic and time-dependent properties. Advanced approaches, including the integration of Magnetic Resonance Imaging (MRI) for 3D displacement fields, further expand VFM's capabilities, allowing for the characterization of opaque materials and complex geometries [7]. In [8] the authors propose a novel method for characterizing elastomeric materials using a

* Corresponding author.
*Email address:* marcin.t.nowak@put.poznan.pl (M. Nowak).

https://doi.org/10.1016/j.compstruc.2026.108356
Received 23 February 2026; Accepted 30 June 2026
Available online 4 July 2026

single heterogeneous mechanical test, where displacement and strain fields are measured with Digital Image Correlation and analyzed via the Virtual Fields Method. A custom-designed apparatus, adaptable to a standard tensile machine, enables simultaneous uniaxial tension, pure shear, and equibiaxial tension states within a single sample. While VFM is a well known method, other approaches such as the Finite Element Model Updating (FEMU) method can also be successfully applied for identifying material parameters [9]. There are also several approaches such as the Equilibrium Gap Method [10] and Subglobal Equilibrium Method [11] which are based on the fundamental concept of the balance between internal and external forces in a continuum. While significant progress has been made in the VFM, there is a growing interest in data-driven approaches that complement traditional techniques. One promising direction is the integration of machine learning with VFM, offering greater flexibility and adaptability in material model identification. In [12] the authors developed a method that integrates VFM with a machine learning framework (NN-EUCLID) to identify constitutive models of biological tissues from 3D full-field displacement data. By formulating loss functions through the VFM rather than the local equilibrium gap, it effectively handles difficulties—such as unknown boundary conditions—and enables accurate identification of both isotropic and anisotropic hyperelastic models.

Despite significant advancements in the application of the Virtual Fields Method (VFM) for material characterization, several challenges remain. The selection of appropriate virtual fields is still an open issue, affecting the accuracy and reliability of the method. One of the proposed solutions to overcome these difficulties is the methodology proposed in [13]. The proposed method enhances the VFM by introducing a grading procedure that selects virtual fields with minimal sensitivity to random noise in full-field experimental data. By analytically deriving the uncertainty in identified material parameters, it ensures more robust identification of anisotropic elastic constants, as demonstrated through numerical and experimental validation. In addition to the appropriate definition of virtual fields, the formulation of equations for new material models requires further refinement to better capture complex mechanical behaviors. The computational aspects related to the integration of VFM can be improved to enhance efficiency and robustness. Recent works have addressed some of these limitations through regularization strategies [14] and by integrating data-driven constitutive modelling frameworks, such as neural networks trained indirectly via the VFM [15]. These developments highlight both the versatility of the VFM and the need for continued research to fully realize its potential in advanced material characterization.

In this work, the Virtual Fields Method is applied to the identification of hyperelastic material constants for polymers in their as-received state, namely unaffected by any prior deformation. This means that the investigated elastic parameters of the examined polyurethane correspond with the primary mechanical characteristics of the material, not altered according to the Mullins effect, which is typical for highly deformable polymers.

The study is carried out under large-deformation conditions and employs a newly designed T-shaped specimen, which generates nonuniform strain fields from the very beginning of loading. To address the challenges associated with such conditions, two modifications are proposed. The first involves an integration scheme for the virtual field equations based on Voronoi-cell discretization, while the second concerns the modification of the VFM through the random generation of virtual fields in accordance with kinematically admissible requirements. The developed implementation is verified through finite element simulations and subsequently applied to determine material parameters for a tested material.

## 2. Virtual fields method for large deformations

The core element of the Virtual Fields Method is to use the weak formulation of the problem of elasticity provided by the Principle of Virtual Work–stress tensor components involved in the mathematical formulation of this principle are meant to be expressed in terms of 1) chosen measures of deformation (strain, elongation etc. obtained from the full-field DIC measurement) and 2) constant parameters determining the mechanical properties of the considered material via constitutive relations, which should be assumed in advance. The resultant equation depends on measured displacements and unknown parameters as well as on the chosen virtual field. The equality of virtual work of external forces and virtual work of internal forces may be written down multiple times, each time using a different virtual displacement field. If these fields are chosen in an appropriate way, the obtained equations are linearly independent. If, additionally, the number of such virtual fields is the same as the number of unknown elastic constants, a system of independent algebraic equations may be created and values of these unknown material parameters may be found as a solution of this system. In the case when the constitutive relations (even those for non-linear elasticity) depend linearly on material parameters, the obtained system of equations is also linear–otherwise a system of non-linear algebraic equations must be considered.

The Principle of Virtual Work (PVW) can be extended to account for large deformations, facilitating the identification of parameters that govern constitutive equations for hyperelastic materials. The derivation of the PVW in the case of finite strains differs from its geometrically linear counterpart in two aspects. First, it is necessary to distinguish between the reference and current configurations of the body, as well as between the material and spatial descriptions using Lagrange and Euler coordinates, respectively. Second, a more general nonlinear measure of deformation must be introduced instead of the Cauchy small strain tensor (a symmetric part of the displacement gradient) in order to account for large deformations. As a result more general tensorial measures of stress, which are appropriate for the finite strain theory, are employed in the PVW formulation.

Let us consider a hyperelastic body (see Fig. 1) occupying a region $V$ in the reference configuration that is bounded by a closed surface $S = S_u \cup S_q$, where $S_q$ is the loaded part of the boundary on which static boundary conditions are prescribed, while $S_u$ is the supported part of the boundary on which kinematic boundary conditions are prescribed.

According to the PVW, homogeneous equilibrium equations and static boundary conditions are satisfied if and only if the virtual work of internal forces is equal to the virtual work of external forces for any virtual displacement field $\mathbf{U}^*$. This statement may be expressed analytically in a number of ways, depending on the choice of the description used (Lagrangian or Eulerian) as well as on the choice of the tensorial measure of stress. Let us consider the Lagrangian description with the reference configuration being the domain for the functions describing the state of the body. After employing the general procedure outlined in [1], the final form of the PVW in the reference configuration may be written down using the 1st Piola–Kirchhoff stress tensor $\mathbf{\Pi}$ in the following way:

$$\int_V \Pi_{ij} U^*_{i,j} \, dV = \int_S \Pi_{ij} N_j U^*_i \, dS \quad \forall U^*_i \tag{1}$$

where $\mathbf{N}$ is the outward unit normal vector of the boundary $S$. The above statement of the PVW accounts for the geometrical nonlinearity. If, in addition, the virtual displacement field is assumed to be kinematically admissible, namely, that it satisfies the homogeneous kinematic boundary conditions prescribed over $S_u$, then the integration of the surface integral in Eq. (1) should be carried out only over the boundary $S_q$.

Virtual Fields Method utilizes the PVW in its two-dimensional variant, due to the nature of DIC measurements on which it is based. In such a case, the general Eq. (1) takes the following form:

$$\int_{S_0} \Pi_{ij} U^*_{i,j} \, dS = \int_{\partial S_0} \Pi_{ij} N_j U^*_i \, dL \quad \forall U^*_i \tag{2}$$

As regards the physical non-linearity of a general finite strain theory of elasticity, we shall focus on isotropic hyperelastic materials for which

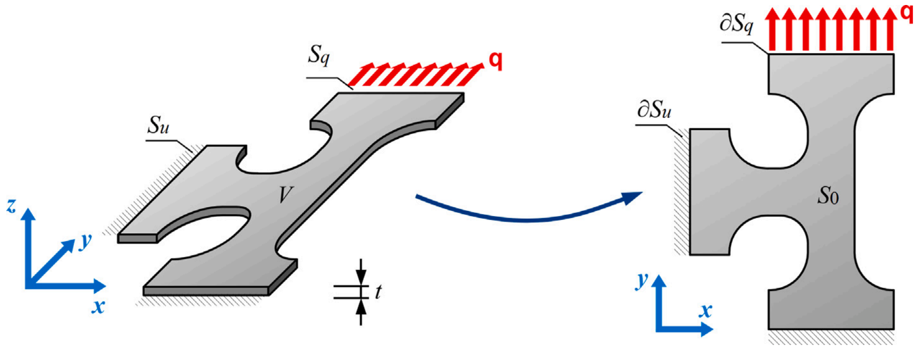


**Fig. 1.** Reference configuration.

an elastic potential exists in the form of the elastic strain energy density function $W$, such that

$$\sigma_{ij} = \frac{2}{J} B_{ik} \frac{\partial W(\mathbf{B})}{\partial B_{kj}} = \frac{2}{J} \left\{ \left[ \left( \frac{\partial W}{\partial I_1} + I_1 \frac{\partial W}{\partial I_2} \right) \mathbf{B} - \frac{\partial W}{\partial I_2} \mathbf{B}^2 \right] + J^2 \frac{\partial W}{\partial I_3} \mathbf{1} \right\} \tag{3}$$

where $\boldsymbol{\sigma}$ stands for the Cauchy true stress tensor, $\mathbf{B}$ is the left Cauchy – Green deformation tensor, $J = \det(\mathbf{F})$ is the determinant of the material deformation gradient, a measure of volumetric deformation, and $I_1, I_2$ and $I_3$ are the invariants of $\mathbf{B}$:

$$\begin{aligned} I_1 &= \lambda_1^2 + \lambda_2^2 + \lambda_3^2 \\ I_2 &= \lambda_2^2\lambda_3^2 + \lambda_3^2\lambda_1^2 + \lambda_1^2\lambda_2^2 \\ I_3 &= J^2 = \lambda_1^2\lambda_2^2\lambda_3^2 \end{aligned} \tag{4}$$

In the above relations $\lambda_i$ $(i = 1, 2, 3)$ are the principal stretches, the eigenvalues of $\mathbf{B}$. If an assumption on incompressibility of the material is made – which is a common approach in modeling of polymers – the volumetric deformation is zero and $J = 1$. Then the general form of the constitutive relations (3) may be rewritten as follows:

$$\sigma_{ij} = -p\delta_{ij} + 2B_{ik} \frac{\partial W(\mathbf{B})}{\partial B_{kj}} \tag{5}$$

where $p$ is an undetermined hydrostatic pressure (locally any value of $p$ may be superimposed as it results in no additional deformation and $p$). The above expression, together with Eq. (4) enable finding the formulas for the eigenvalues of the true stress tensor $\boldsymbol{\sigma}$:

$$\sigma_i = -p + \lambda_i \frac{\partial W}{\partial \lambda_i} \quad i = 1, 2, 3 \quad \text{(no summation over } i\text{!)} \tag{6}$$

Our research is focused on the Mooney – Rivlin hyperelastic solid, as it is one of the simplest hyperelastic models and one of the most commonly used constitutive model in practical computation. This choice is motivated by the need to ensure a robust and well-posed inverse identification problem while retaining sufficient nonlinear elastic behaviour within the considered deformation range. This material model is characterized by the following strain energy density function:

$$W = \sum_{p=0}^{N} \sum_{q=0}^{N} C_{pq} (\bar{I}_1 - 3)^p (\bar{I}_2 - 3)^q + \sum_{m=1}^{Q} \frac{1}{D_m} (J - 1)^{2m} \tag{7}$$

in which $N, M, C_{pq}, D_m$ $(m, n = 0, 1, 2, \dots\ N, m = 1, \dots, M)$ are material parameters, $C_{00} = 0$ and modified invariants of deformation tensors are defined as $\bar{I}_1 = J^{-2/3} I_1$, $\bar{I}_2 = J^{-4/3} I_2$.

Furthermore, we narrow our considerations to the most commonly used variant of the above proposition, namely a two-parameter incompressible Mooney-Rivlin material which is obtained after taking $N = 1$ $C_{11} = 0$ and disregarding the volumetric deformation terms:

$$W = C_1(\bar{I}_1 - 3) + C_2(\bar{I}_2 - 3) \tag{8}$$

For notational simplicity, the parameters $C_{10}$ and $C_{01}$ are hereafter denoted as $C_1$ and $C_2$, respectively. For incompressible materials there is no volumetric deformation, so $J = dV/dV_0 = 1$. As a result isochoric invariants of deformation tensors are equal to the regular invariants, namely $\bar{I}_1 = I_1$ and $\bar{I}_2 = I_2$. Making use of these relations, we may notice that for incompressible materials $\bar{I}_2 = I_2 = \sum_{i=1}^{3} \lambda_i^{-2}$ and the Eq. (6) for the above form of the strain density function $W$ takes the following form:

$$\sigma_i = -p + 2\left( C_1\lambda_i^2 - C_2\frac{1}{\lambda_i^2} \right) \quad i = 1, 2, 3 \tag{9}$$

Assumption of the plane stress state gives us a condition $\sigma_3 = 0$ which enables to determine the unknown hydrostatic pressure:

$$p = 2\left( C_1\lambda_3^2 - C_2\frac{1}{\lambda_3^2} \right) \tag{10}$$

Then we may finally write:

$$\sigma_i = 2\left[ C_1\left(\lambda_i^2 - \lambda_3^2\right) - C_2\left( \frac{1}{\lambda_i^2} - \frac{1}{\lambda_3^2} \right) \right] \quad i = 1, 2 \tag{11}$$

The components of the Cauchy stress tensor in the original coordinate system may be found with the use of the tensorial transformation law, which takes the following form for the 2nd rank tensors:

$$\sigma_{ij} = A_{ik} A_{jl} \sigma'_{kl} \tag{12}$$

where $\sigma'_{11} = \sigma_1$, $\sigma'_{22} = \sigma_2$, $\sigma'_{33} = \sigma_3 = 0$, $\sigma'_{ij} = 0$ for $i \neq j$ and $A_{ij}$ are the components of the transformation matrix from the system of principal axes of the Cauchy stress tensor to the original coordinate system.

$$A_{ij} = \mathbf{e}_i \cdot \mathbf{b}_j \tag{13}$$

where

- $\mathbf{e}_i$ – $i$-th basis vector of the original coordinate system: $\mathbf{e}_j = [\delta_{1j}; \delta_{2j}; \delta_{3j}]$
- $\mathbf{b}_j$ – $j$-th eigenvector of the Cauchy stress tensor

It is now possible to express the components of the PK1 stress tensor $\Pi$ in terms of principal elongations using the following relation:

$$\Pi_{ij} = J\sigma_{ik} F^{-1}_{jk} \tag{14}$$

Finally, we get

$$\Pi_{ij} = C_1\Theta_{ij} + C_2\Lambda_{ij} \tag{15}$$

where

$$\begin{cases} \Theta_{11} = \frac{2}{D}\left[(\lambda_1^2 - \lambda_3^2)(A_{11}^2F_{22} - A_{11}A_{21}F_{12}) + (\lambda_2^2 - \lambda_3^2)(A_{12}^2F_{22} - A_{12}A_{22}F_{12})\right] \\ \Theta_{12} = \frac{2}{D}\left[(\lambda_1^2 - \lambda_3^2)(-A_{11}^2F_{21} + A_{11}A_{21}F_{11}) + (\lambda_2^2 - \lambda_3^2)(-A_{12}^2F_{21} + A_{12}A_{22}F_{11})\right] \\ \Theta_{21} = \frac{2}{D}\left[(\lambda_1^2 - \lambda_3^2)(-A_{21}^2F_{12} + A_{11}A_{21}F_{22}) + (\lambda_2^2 - \lambda_3^2)(-A_{22}^2F_{12} + A_{12}A_{22}F_{22})\right] \\ \Theta_{22} = \frac{2}{D}\left[(\lambda_1^2 - \lambda_3^2)(A_{21}^2F_{11} - A_{11}A_{21}F_{21}) + (\lambda_2^2 - \lambda_3^2)(A_{22}^2F_{11} - A_{12}A_{22}F_{21})\right] \end{cases} \tag{16}$$

$$
\begin{cases}
\Lambda_{11} = -\frac{2}{D}\left[\left(\frac{1}{\lambda_1^2}-\frac{1}{\lambda_3^2}\right)\left(A_{11}^2F_{22}-A_{11}A_{21}F_{12}\right)\right. \\
\left. +\left(\frac{1}{\lambda_2^2}-\frac{1}{\lambda_3^2}\right)\left(A_{12}^2F_{22}-A_{12}A_{22}F_{12}\right)\right] \\
\Lambda_{12} = -\frac{2}{D}\left[\left(\frac{1}{\lambda_1^2}-\frac{1}{\lambda_3^2}\right)\left(-A_{11}^2F_{21}+A_{11}A_{21}F_{11}\right)\right. \\
\left. +\left(\frac{1}{\lambda_2^2}-\frac{1}{\lambda_3^2}\right)\left(-A_{12}^2F_{21}+A_{12}A_{22}F_{11}\right)\right] \\
\Lambda_{21} = -\frac{2}{D}\left[\left(\frac{1}{\lambda_1^2}-\frac{1}{\lambda_3^2}\right)\left(-A_{21}^2F_{12}+A_{11}A_{21}F_{22}\right)\right. \\
\left. +\left(\frac{1}{\lambda_2^2}-\frac{1}{\lambda_3^2}\right)\left(-A_{22}^2F_{12}+A_{12}A_{22}F_{22}\right)\right] \\
\Lambda_{22} = -\frac{2}{D}\left[\left(\frac{1}{\lambda_1^2}-\frac{1}{\lambda_3^2}\right)\left(A_{21}^2F_{11}-A_{11}A_{21}F_{21}\right)\right. \\
\left. +\left(\frac{1}{\lambda_2^2}-\frac{1}{\lambda_3^2}\right)\left(A_{22}^2F_{11}-A_{12}A_{22}F_{21}\right)\right]
\end{cases}
\tag{17}
$$

where $D = F_{11}F_{22} - F_{12}F_{21}$

or in a more compact form (summation over $k, m, n = 1, 2$):

$$
\Theta_{ij} = 2J\,A_{im}A_{kn}F_{jk}^{-1}\left[\sum_{l=1}^{2}\left(\lambda_l^2-\lambda_3^2\right)\delta_{ml}\delta_{nl}\right] \quad i,j=1,2 \tag{18}
$$

$$
\Lambda_{ij} = 2J\,A_{im}A_{kn}F_{jk}^{-1}\left[\sum_{l=1}^{2}\left(\frac{1}{\lambda_l^2}-\frac{1}{\lambda_3^2}\right)\delta_{ml}\delta_{nl}\right] \quad i,j=1,2 \tag{19}
$$

This result has already been reported in [1,8]. Only a slight correction should be made in these previously presented solutions, namely that the squared component of the transformation matrix in the second round bracket in expressions for $\Theta_{22}$ and $\Lambda_{22}$ should be $A_{21}$ instead of $A_{12}$. Fortunately, this small error (surely a typo) has no impact on calculations, since in two-dimensional problems we have $A_{12} = -A_{21}$ and so $A_{12}^2 = A_{21}^2$.

Finally, using the PVW Eqs. (2), a system of two linear equations for the unknown material parameters $C_1$ and $C_2$ may be written in the following form, according to the VFM:

$$
\begin{cases}
C_1\int_S \mathbf{\Theta}\cdot\frac{\partial \mathbf{U}_1^*}{\partial \mathbf{X}}dS + C_2\int_S \mathbf{\Lambda}\cdot\frac{\partial \mathbf{U}_1^*}{\partial \mathbf{X}}dS = \int_{\partial S}\mathbf{q}\cdot\mathbf{U}_1^* dL \\
C_1\int_S \mathbf{\Theta}\cdot\frac{\partial \mathbf{U}_2^*}{\partial \mathbf{X}}dS + C_2\int_S \mathbf{\Lambda}\cdot\frac{\partial \mathbf{U}_2^*}{\partial \mathbf{X}}dS = \int_{\partial S}\mathbf{q}\cdot\mathbf{U}_2^* dL
\end{cases}
\tag{20}
$$

where $\mathbf{U}_1^*$ and $\mathbf{U}_2^*$ are two chosen virtual displacement fields.

Fig. 2. Poured polymer sheets and PS adhesive components prepared for mixing.

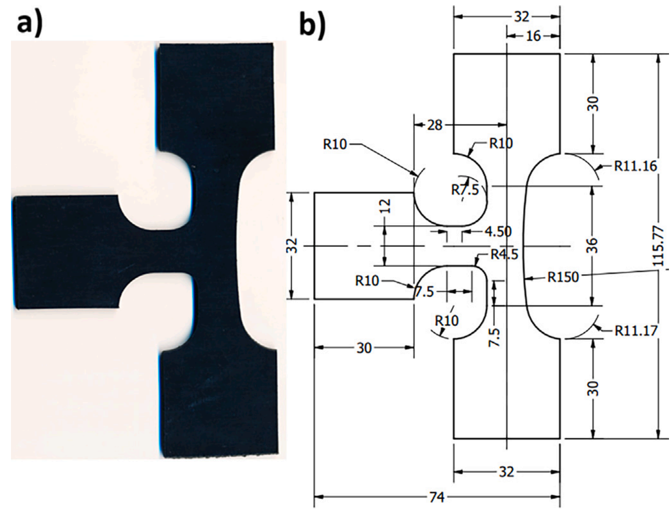


Fig. 3. The T-shaped sample (a) and its dimensions in milimiters (b) cut out from the rectangular sheets of 2.3 mm thickness.

## 3. Materials and methods

This section presents the materials, numerical procedures, and experimental methods employed in this study. First, the properties of the investigated polyurethane material are described. Subsequently, the calibration and verification of the Virtual Fields Method algorithm are detailed, including the numerical implementation and selection of virtual fields. Finally, the experimental setup and testing procedures used to validate the proposed framework are introduced.

### 3.1. Material

The material studied in this paper is the elastic polyurethane PS which exhibits hyperelastic characteristics [16,17]. The material was provided by FlexAndRobust Systems sp. z o. o., Poland. It was found to be an effective medium in the strengthening and repair of masonry, [18] reinforced concrete [19,20] and timber-concrete composite structures [21,22].

The material used to prepare the sample was delivered in the form of flat rectangular sheets, of approximately A4 size (210 × 297 mm) and 2.3 mm thickness. The PS is a solvent-free, elastic, two-component, polyurethane-based adhesive able to provide a more uniform stress distribution compared to conventional rigid connectors. In order to investigate its mechanical performance in a controlled manner, the raw material was processed and prepared into test specimens as described below. The adhesive components were mixed according to the manufacturer's technical data sheet, following a prescribed weight ratio of component A to B equal to 100:11. The mixing process involved the initial combination of both components in a plastic container (see Fig. 2), after which the mixture was transferred to a second container and further mixed for 10 s prior to application into the mould. This procedure was employed to ensure a homogeneous blend, which is critical for achieving consistent material properties such as mechanical strength. The adhesive was mixed for approximately 120 s until a uniform consistency was obtained, taking care not to introduce air into the mixture. The mechanical mixing speed was 600 – –800 rpm. All specimens were cured

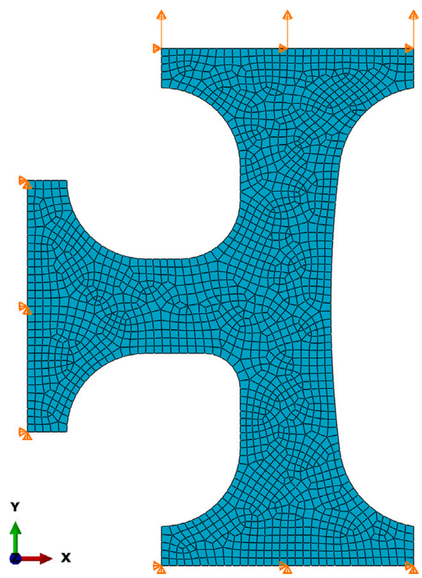


**Fig. 4.** FE model of T-shape sample under tension created in Abaqus/CAE.

for 21 days in a room with a stable temperature of 20°C and relative humidity of 65% ± 5%.

Polyurethane F&R®PS was initially prefabricated in the form of strips 210 mm wide and 950 mm long in the special rubber forms with a 2 mm high frame. They were then cut into smaller rectangular sheets of a size approximately equivalent to A4 paper. Due to the relatively large dimensions of the mould used for the production of the adhesive strips, differences in thickness along the length of the samples were observed–this created the need for levelling the surface using a steel spatula. After curing, the T-shaped samples presented in Fig. 3 were cut out from the A4 sheets of the polymer.

The final shape of the presented sample was inspired by the T-shaped specimen proposed in the theoretical work by Guélon et al. [8] and was determined through a systematic optimization procedure aimed at improving the accuracy of VFM for material parameter identification. Four key geometric parameters of the T-shaped specimen were analyzed, with particular focus on the radii of the rounded corners. A series of possible values for these radii were tested to evaluate their influence on the resulting strain fields and the overall error in VFM calculations. Each combination of the geometric parameters was considered, resulting in a total of 72 analyzed cases. The optimal shape was selected based on the configuration that minimized the discrepancy between the assumed and predicted material constants used in a Finite Element benchmark model, which was utilized in order to numerically mimic a DIC measurement–a more detailed description of this approach may be found in the following section.

### 3.2. Calibration of the VFM algorithm

A verification process based on finite element analysis (FEA) was conducted to ensure the accurate implementation of the VFM algorithm and to evaluate the error associated with the results derived from the VFM method. Simulated experimental data were generated using FEM analysis of a hyperelastic material with predefined constitutive parameters, which mimic the results of the DIC method. To achieve this, DIC data points were represented by the nodal displacements from the FE model. The developed algorithm was then applied to extract material constants and assess the method's accuracy by comparing the computed values to the known hyperelastic constants used in the benchmark FEM model. While any deformation process could theoretically serve as validation, the T-shaped specimen was selected for consistency. The hyperelastic material parameters used in the simulation for the Mooney–Rivlin model were assumed to be $C_1 = 10$ MPa and $C_2 = 20$ MPa. The FEM model was created using the Abaqus/CAE software. The adopted geometry and discretization, along with the applied boundary conditions, are presented in Fig. 4. The boundary conditions correspond to those used in the experiment. The bottom and left edges of the sample were fixed and the prescribed displacement (20 mm) was applied to the top edge of the sample. In the simulation, CPS4R finite elements, i.e., bilinear plane-stress quadrilateral elements with reduced integration, were employed, and the sample thickness was set to 2.3 mm. The influence of mesh density was assessed using two different mesh configurations (coarse and fine). No significant effect of mesh refinement on the obtained results was observed, indicating that the numerical solution is mesh-insensitive within the considered discretization range.

A numerical simulation of a quasi-static tensile test was performed to generate the displacement field. The calculated benchmark fields using

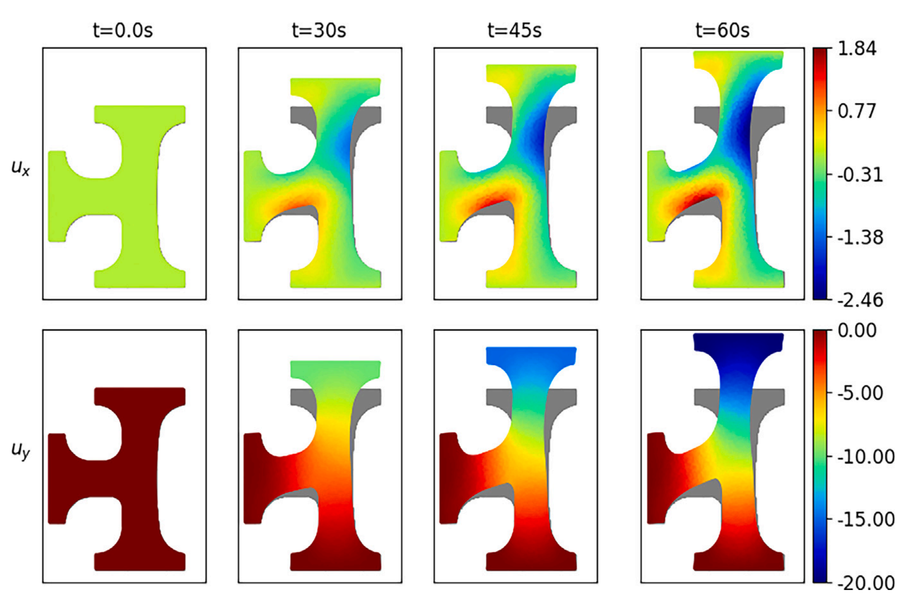


**Fig. 5.** Displacement fields obtained for the assumed hyperelastic material mode using finite element simulation.

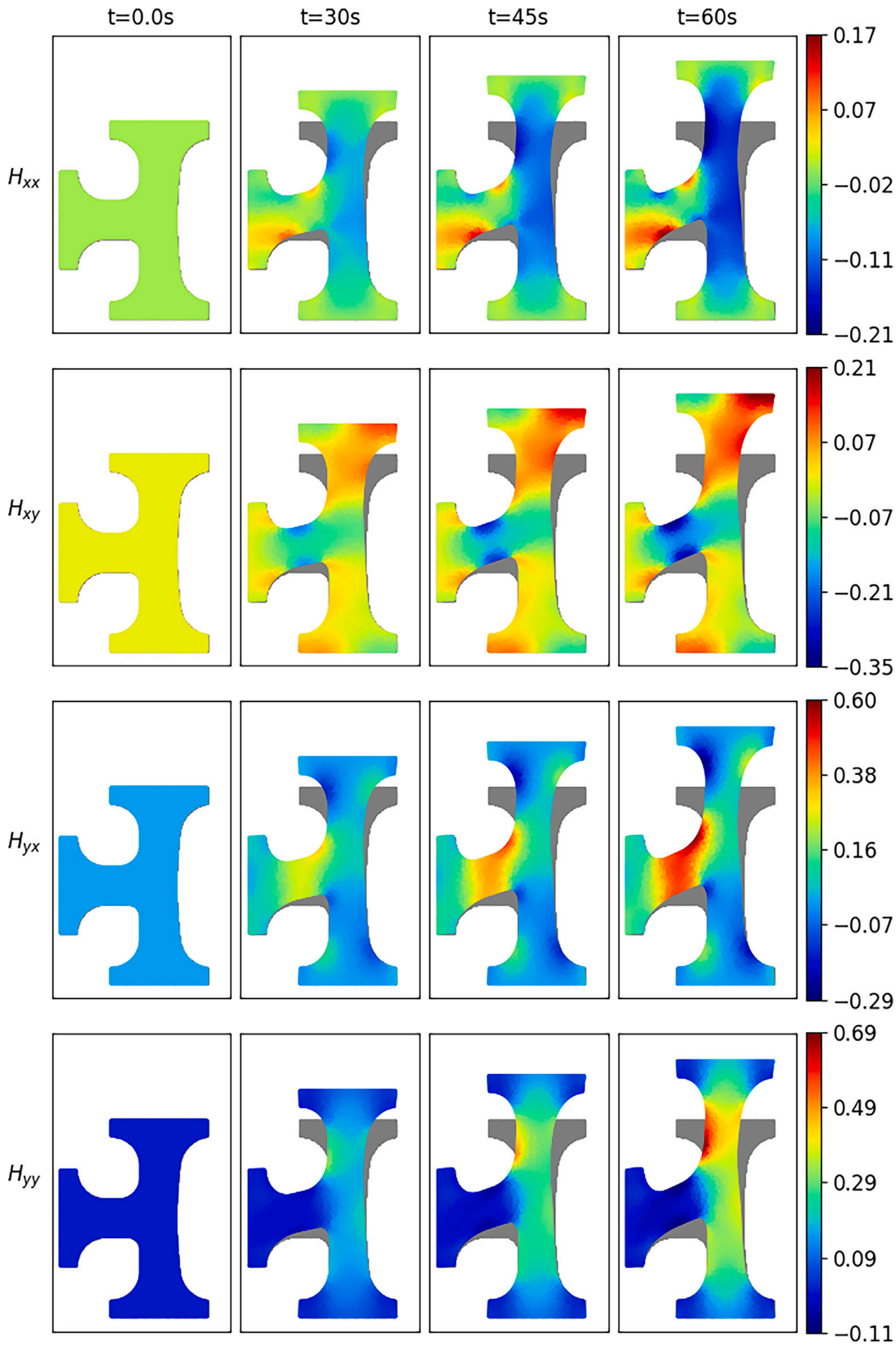


**Fig. 6.** Displacement gradient obtained for the assumed hyperelastic material model in FEM simulation.

Abaqus software are shown in Fig. 5. The figure presents all of the in-plane displacement components at the selected time instances of the deformation process.

It is important to note that only the displacement vector field $\boldsymbol{u}$ was extracted from the simulation results. The displacement gradient $\boldsymbol{H} = \boldsymbol{u} \otimes \nabla$ was calculated in Thermocorr DIC software using a polynomial approximation of the local neighbourhood of material points [23]. The results of the displacement gradient calculations are presented in Fig. 6. As expected, the distribution of the displacement gradient components is non-uniform, and a change of sign is observed. This indicates that the material undergoes local compression and extension.

From the result file of the numerical simulation, the history of the macroscopic force was also extracted. The value was calculated as the sum of the nodal reaction forces on the top edge of the sample. Fig. 7 presents the horizontal and vertical components of the macroscopic force vector. A slightly nonlinear response is observed due to

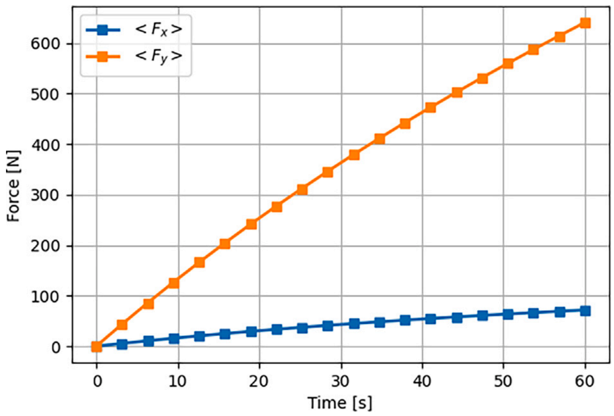


**Fig. 7.** External reaction force calculated from the results of the numerical simulation.

the nonlinear constitutive model. The extracted force history, along with the displacement field and its gradient, serves as input for the verification of the virtual fields method. Since the loading was prescribed under quasi-static conditions with a constant displacement rate, the imposed displacement evolves linearly in time. Therefore, the time axis used in Fig. 7 is strictly equivalent to the imposed displacement, and both representations lead to identical physical interpretation of the force–displacement response.

### 3.2.1. Numerical integration of the virtual work principle equation

The solution of the VFM equations presented in Section 2 requires an integration step. As the fields are available only at discrete points within the domain, the integration is carried out numerically by summing over the corresponding data points. The basic approach, in which the contribution of each point is assumed to be uniform-calculated as the total area of the region of interest (ROI) divided by the number of points-has certain limitations. On one hand, the areas corresponding to boundary points are always overestimated. On the other hand, the areas associated with interior points cannot be accurately determined when the measurement points are nonuniformly distributed. This issue becomes even more pronounced in the deformed configuration, where the distances between neighboring points change during deformation, further affecting the accuracy of the area estimation. To address these limitations, an enhanced approach based on a Voronoi tessellation is proposed, which remains applicable under large deformation kinematics. Fig. 8 shows the analyzed T-shaped specimen together with its initial and deformed configurations. In both cases, the discretization is defined by the set of DIC measurement points, which serve as the basis for the construction of the Voronoi diagram. Each discrete point is assigned a field value corresponding to the measured kinematic quantities. These points originate from the spatial discretization used in the DIC procedure and are consistent with the nodal representation adopted in the finite element model shown in Fig. 4.

In this approach, the ROI boundary is first determined as an ordered array of boundary points (concave hull). This is achieved using Delaunay triangulation with a maximum length constraint, which is linked to the distance between neighboring points in the reference state. The boundary points define the vertices of the boundary polygon. Next, based on the set of the ROI points, a Voronoi diagram is generated and then clipped by the boundary polygon. This results in a bounded Voronoi diagram, where each point in the Virtual Fields Method (VFM) domain is assigned a corresponding Voronoi region. It should be noted that the integration domain is constructed from discrete DIC measurement points, where the spatial resolution and experimental processing inherently limit the accuracy of the reconstructed fields. In particular, each

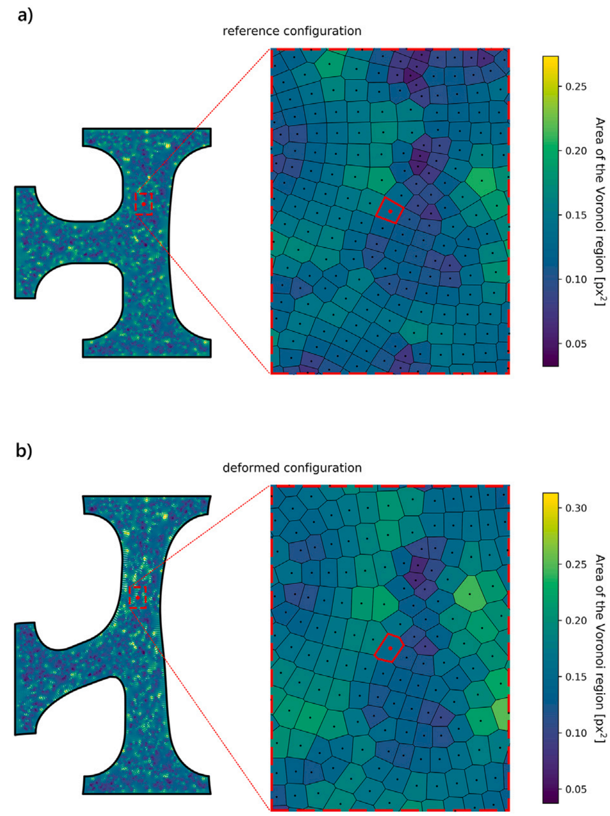


**Fig. 8.** T-shaped sample and its Voronoi tessellation computed on a) the initial configuration, b) the deformed configuration.

DIC point represents a spatially averaged quantity over a finite correlation subset, meaning that the measured fields are already smoothed at the scale of the measurement resolution.

Consequently, in the numerical integration of the virtual work principle equation, the contribution of each point is weighted according to the area of its corresponding Voronoi region. The surface integral was replaced by the following sum:

$$\int_{S_o} (\cdot) d S_0 \approx \sum_{i=1}^{m} (\cdot)_i A_i \tag{21}$$

where $A_i$ is the area of the Voronoi region which corresponds to i-th node of the finite element mesh (in real experiments DIC point) and $m$ is the total number of discrete points.

### 3.2.2. Virtual fields

The selection of virtual fields is a critical step in the VFM. For cases involving small deformations and elasticity, this is typically done using established numerical tools [4]. However, in the present context of large deformations and hyperelasticity, the authors propose a slight modification to this approach. Specifically, a heuristic method is employed, where a large number of randomly generated virtual fields are created. The process of generating virtual fields consists of the following steps. First, the positions of control points are generated based on a rectangular grid. Next, randomly generated displacement vector values are assigned to these control points, introducing variation into the field (Fig. 9).

The final step involves interpolation to determine the values between the control points. For this purpose, interpolation functions using third-degree polynomials from the NumPy library are utilized. This approach ensures smooth transitions and a continuous representation of the field across the entire grid. By using polynomial interpolation, the generated

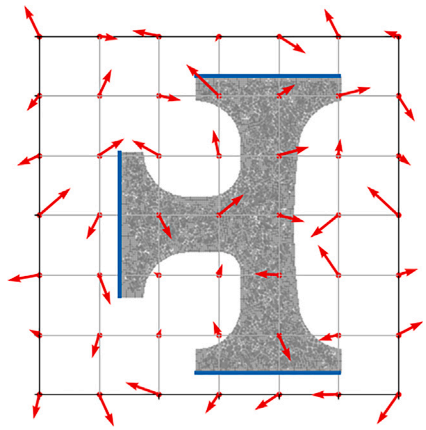

**Fig. 9.** Regular grid points with a randomly generated displacement vector assigned to each point. The blue lines correspond to the boundary points where the displacement vectors are enforced to be consistent with the boundary conditions, ensuring a kinematically admissible displacement field.

virtual field and its gradient maintain continuous variations. Examples of the generated fields are shown in Fig. 10. Although the process is displacement-controlled in the experiment and the kinematic boundary conditions on the upper edge are known, the corresponding horizontal reaction forces are not measured. In the present approach, it is therefore assumed that the resultant reaction force in this direction on the upper edge is negligibly small. Under this assumption, the contribution of this boundary to the external virtual work vanishes, which allows the virtual displacement field to be chosen arbitrarily. Each of the generated fields satisfies the principle of virtual work. Each field provides one equation of the system of Eqs. (20). Using all the fields leads to an overdetermined system. Therefore, in this work, all the fields are used, and the final result is computed using the least-squares method.

### 3.2.3. Results of Algorithm Calibration

The extracted data from Abaqus simulation presented in Section 3.2 were used to mimic the experimental data. The results of the verification process for all postulated virtual fields described in Section 3.2.2 lead to the result presented in Table 1.

**Table 1**
Assumed and identified material parameters of hyperelastic material model based on FE resutls.

| | Assumed | Identified |
|---|---|---|
| $C_1$ [MPa] | 10 | 9.63 |
| $C_2$ [MPa] | 20 | 19.37 |

**Table 2**
Relative error of the identified material parameter for isotropic material model.

| | Voronoi-based int. | Std approach |
|---|---|---|
| $E$ [GPa] | 0.7% | 1.1% |
| $\nu$ [-] | 1.2% | 2.7% |

The comparison between the assumed and identified material parameters demonstrates very good agreement. The relative errors are approximately 3.7% for $C_1$ and 3.15% for $C_2$, confirming the correctness of the implemented VFM algorithm. In addition to validating the overall implementation of the method, the influence of the numerical integration scheme was also examined. The Voronoi-based integration was compared with the standard approach, in which an equal area is assigned to each DIC point. The calculations were performed for an isotropic elastic material with two material constants: Young's modulus $E$ and Poisson's ratio $\nu$. The use of a linear isotropic elastic model in this comparison is intentional, as it allows the influence of the numerical integration scheme to be assessed independently of nonlinear material effects. In this case, the construction of admissible virtual fields is straightforward and does not introduce additional complexities associated with finite-strain formulations.

The results presented in Table 2 confirm that the use of Voronoi-based integration reduces the errors.

### 3.3. Experimental setup

The experimental analysis of the deformation of T-shaped sample was performed in a testing machine equipped with specially designed grips.

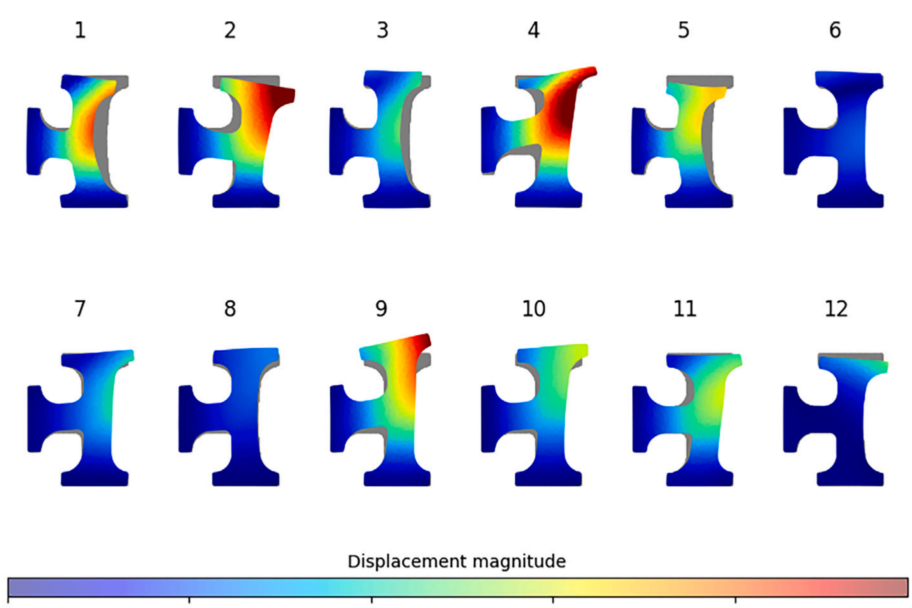


**Fig. 10.** Example of randomly generated virtual fields for a T-shaped sample. The colors correspond to the magnitude of the displacement vector.

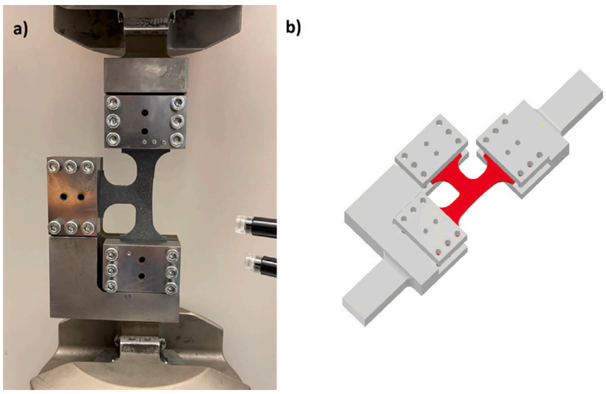


**Fig. 11.** a) the experimental setup for DIC analysis and b) the specially designed grips for the testing machine.

**Table 3**
Parameters of the pco.edge 5.5 visible range camera used in DIC measurements.

| Parameters | Value |
|---|---|
| Resolution [px] | 1810 × 2560 |
| Recording frequency [Hz] | 10 |
| Exposure time [ms] | 1.5 |
| Pixel size [µm] | 21 |

These grips allows to apply controlled loads and boundary conditions allowing to observe complex strain distribution that are not uniform across material. This setup is particularly useful for investigating how different regions of the sample respond to loading, providing valuable data for VFM. The grips and the experimental setup are presented in Fig. 11.

In this setup, the bottom grip is fixed while the upper grip is mobile. The applied displacement rate corresponds to a quasi-static deformation process. The MTS 858 testing machine was used in displacement-controlled uniaxial tension test with a displacement rate of 0.015 mm/s. Due to inhomogeneous deformation of the sample the value of the strain rate was calculated as the average value of strain rate field obtained using DIC method. The calculated values for all studied cases were approximately equal to $1 \times 10^{-4}\ 1/s$. During the tests, the deformation of the sample surface was observed using a pco.edge 5.5 visible-range camera, and a series of grayscale images were captured. The camera settings are specified in Table 3. To create an appropriate speckle pattern for DIC analysis, the small white paint dots were applied to the specimen's surface.

## 4. Identification of material parameters

This section presents the identification of material parameters based on full-field displacement data obtained from Digital Image Correlation (DIC) measurements. The Virtual Fields Method (VFM) is applied to a T-shaped polyurethane specimen, which generates a heterogeneous deformation field suitable for inverse identification under large strain conditions. The obtained results are subsequently analyzed and compared with independent uniaxial tension tests to assess the consistency of the identified constitutive parameters.

### *4.1. Application of the VFM to the DIC measurement of t-shape sample deformation*

The virtual field method was used to identify material constants for the material described in Section 3.1. The structural characteristics of the material suggest that it can be modelled in the elastic range using a hyperelastic material model–a two-parameter incompressible Mooney–Rivlin material model was assumed. Following the steps of the VFM method, the displacement field obtained using the DIC method as well as the macroscopic response of the studied material are shown in Figs. 12 and 13.

Using the same gradient evaluation method as described in Section 3.2, the computed results for the measured displacement field are presented in Fig. 14. The highest strain concentrations occur near the grips, where the specimen transitions into the clamping section. All components of the displacement gradient field exhibit non-uniformity. The results of the calculations yielded the following values for the two material constants: $C_1 = -5.023$ MPa and $C_2 = 9.103$ MPa.

The obtained result requires a comment. Not all numerical values of elastic parameters are admissible either from a purely theoretical or practical (computational) point of view. In particular, local existence, local uniqueness and regularity of the solution of the boundary value problem may be guaranteed–under appropriate assumptions–by satisfying the strong ellipticity condition. Loss of ellipticity may also result in a lack of convergence of Finite Element Method simulations as well as severe mesh dependency of the obtained solutions. The strong ellipticity condition requires that the acoustic tensor should be positive definite for any wave propagation direction and any wave polarization vector, resulting in real and positive wave propagation velocities. A detailed discussion on the strong ellipticity conditions may be found in [24]. In the case of isotropic hyperelastic materials it may be shown that the consequence of strong ellipticity is that the following Baker–Ericksen inequalities must hold true:

$$(\sigma_i - \sigma_j)(\lambda_i - \lambda_j) > 0\,, \quad i,j = 1,2,3\,,\ (i \neq j) \tag{22}$$

It is important to note that while the above inequalities are necessary conditions derived from strong ellipticity, they are not sufficient conditions, namely they do not imply strong ellipticity.

In the case of the considered two-parameter incompressible Mooney-Rivlin hyperelastic material, according to Eq. (9), the above inequalities can be expressed in the following form:

$$\begin{cases} C_1 + \lambda_1^2 C_2 > 0 \\ C_1 + \lambda_2^2 C_2 > 0 \\ C_1 + \lambda_3^2 C_2 > 0 \end{cases} \tag{23}$$

This condition is satisfied for all possible magnitudes of principal stretches ($\lambda_i > 0$) if and only if both $C_1 > 0$ and $C_2 > 0$. Within the range of small strains ($\lambda_i \approx 1$), the above inequalities simplify to

$$\frac{G_0}{2} = C_1 + C_2 \geq 0 \tag{24}$$

which is a restriction imposed on the initial tangent shear modulus $G_0$. In the case of finite strains $C_1 < 0$ or $C_2 < 0$ necessarily makes the Baker-Ericksen inequality fail under certain deformation conditions, what implies the loss of strong ellipticity. For $C_2 < 0$ the strong ellipticity condition may still be satisfied if the material does not undergo severe deformation, namely, if the principal stretches do not take extreme values such as $\lambda_i \to 0$ or $\lambda_j \to \infty$. On the other hand, if $C_1 < 0$, the strong ellipticity condition will always eventually fail for sufficiently large deformation.

For $C_1 = -5.023$ MPa and $C_2 = 9.103$ MPa, in the case of simple tension of an incompressible solid, for which

$$\left(\lambda_2 = \lambda_3 = \frac{1}{\sqrt{\lambda_1}}\right)$$

The Baker–Ericksen inequality fails for a relative elongation $\varepsilon = \lambda - 1 \approx 81.23\%$. In fact, the mechanical characteristics of such a material lose their physical significance for $\varepsilon \approx 35.83\%$ beyond which the material softens, which is not observed in reality. While the limited range of allowable strain, for which the strong ellipticity condition is

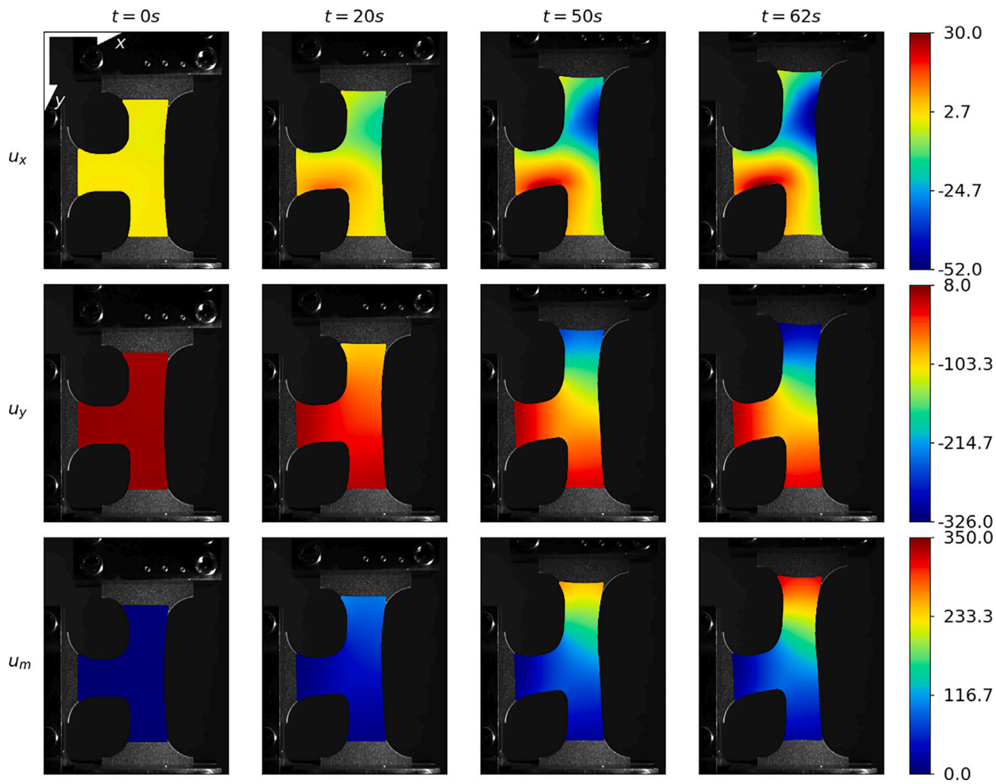


**Fig. 12.** Results of DIC analysis (the components of the displacement vector $u_x$, $u_y$ and $u_m$ - magnitude of the displacement vector) for given time instances.

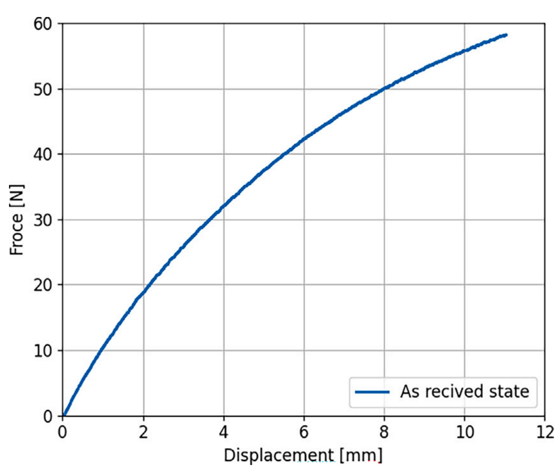


**Fig. 13.** The force-displacement curve measured using a testing machine for the T-shaped sample.

satisfied, may be considered unacceptable from the theoretical point of view, one should notice that an average strain at break recorded for the PS polyurethane for the strain rate $\dot{\varepsilon} = 10^{-1}1/\min$ is ca. 28.02%. However, for higher strain rates a relative elongation at break is even more than 60%. In such cases the proposed constitutive model should be disregarded.

In the case of a simple shear state

$$\lambda_{1/2} = \sqrt{1 + \frac{\gamma}{2}\left(\gamma \pm \sqrt{\gamma^2 + 4}\right)}, \quad \lambda_3 = 1$$

where $\gamma = u/t$, $u$ stands for shear displacement and $t$ is the thickness of the sheared adhesive layer, the Baker-Ericksen inequality fails for $\gamma \approx 60,34\%$. This is against experimental evidence–independent research (to be published) involving strength tests on sheared single lap joints indicates that the PS polyurethane may undergo severe distortional strain up to $\gamma \approx 150\%$.

The limited applicability of the obtained result may perhaps be explained with an over-simplified character of the two-parameter incompressible Mooney–Rivlin hyperelastic material model. Future research should focus on the use of more sophisticated constitutive models.

### 4.2. Uniaxial tension test on dumb-bell specimens

To compare the identification results from the Virtual Fields Method, uniaxial tension tests were conducted using a Zwick/Roell 1455 Universal Testing Machine. The experimental results provide stress-strain curves obtained by measuring the force using the testing machine and the axial displacement. The geometry of the specimen is shown in Fig. 15. The specimen corresponds to a standard Type 1A geometry in accordance with ISO 527. This standardized geometry ensures uniform stress distribution and enables reliable comparison of uniaxial tensile test results. The obtained stress-strain curves are shown in Fig. 16. It can be observed that the stress–strain responses corresponding to all three strain rates are nearly identical. The curves show no significant differences in stiffness or overall mechanical behavior. Therefore, it can be concluded that the material does not exhibit noticeable strain-rate sensitivity within the investigated range of strain rates.

### 4.3. Comparison of obtained results

The material parameters identified using the proposed T-shaped VFM approach were validated through comparison with the experimental stress–strain curves presented in the previous section. To this end, the identified parameters were used to predict the theoretical uniaxial response of the material. For the assumed hyperelastic model, the constitutive relation under uniaxial tension reduces to the following

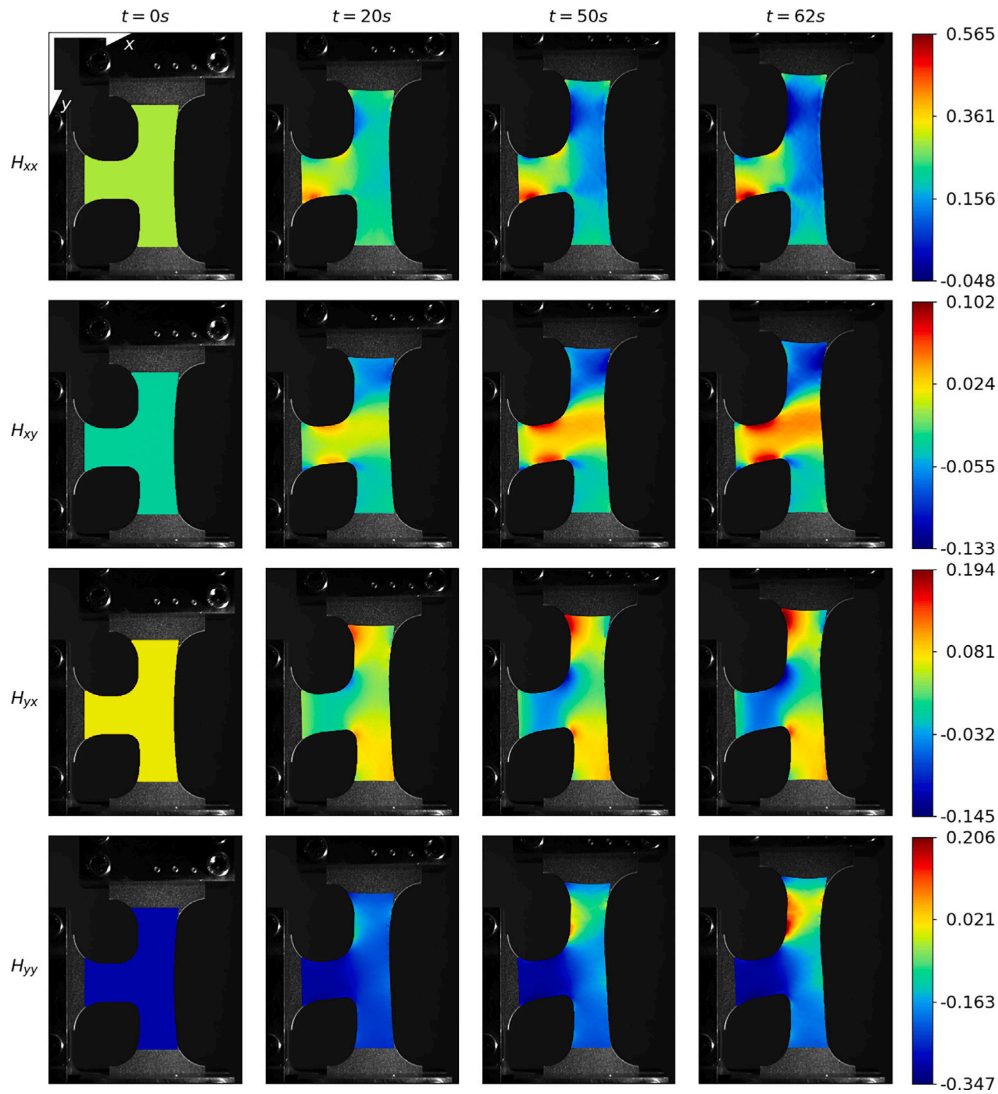


**Fig. 14.** Results of DIC analysis (the components of the displacement gradient tensor $H_{xx}$, $H_{xy}$, $H_{yx}$ and $H_{yy}$) for given time instances.

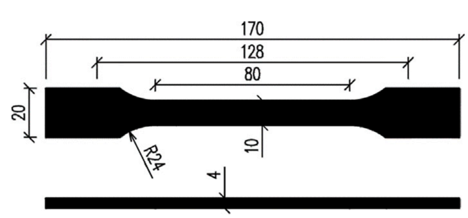


**Fig. 15.** Geometry of the specimen for uniaxial tensile testing. All dimensions are in mm.

one-dimensional form:

$$\sigma(\varepsilon) = 2C_1\left((\varepsilon+1)^2 - \frac{1}{(\varepsilon+1)}\right) + 2C_2\left((\varepsilon+1) - \frac{1}{(\varepsilon+1)^2}\right) \tag{25}$$

where $\sigma$ denotes the Cauchy (true) stress and $\varepsilon$ represents the engineering strain. Eq. (25) was used to assess how accurately the assumed material model, together with the identified parameters, predicts the tensile response. Fig. 17 presents the experimental uniaxial tension data as a shaded gray region, along with the curve computed using Eq. (25). The predicted response obtained using the proposed T-shaped VFM approach lies well within the experimental range. It should be noted that the accuracy of the identified response may depend on the quality of the input experimental data, including possible measurement noise, and a more detailed uncertainty analysis would be required for a rigorous assessment of the robustness of the proposed identification procedure.

## 5. Summary and conclusions

Presented research was focused on the practical application of the Virtual Fields Method in the identification of material parameters of a highly deformable two-component polyurethane adhesive. Among the most notable issues discussed in this article one should mention the following:

- A new experimental setup was developed to analyze materials under nonhomogeneous deformation conditions.
- A specially designed T-shaped specimen was created to generate the desired strain distribution. Appropriate machine grips were also designed and manufactured in order to ensure kinematic boundary conditions for the T-shaped specimens.
- An algorithm based on the Virtual Fields Method (VFM) was developed for the analysis of hyperelasticity. Instead of solving a

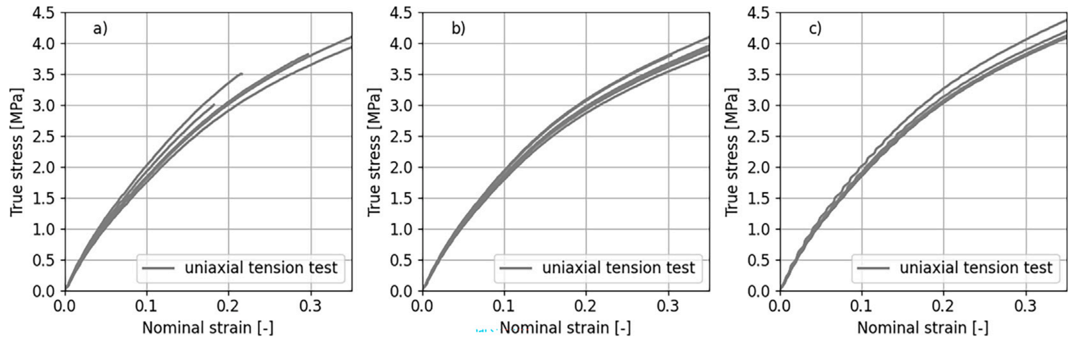


**Fig. 16.** Stress-strain curves for uniaxial tension obtained for different strain rates a) $\dot{\varepsilon} = 10^{-1}\ 1/\min$, b) $\dot{\varepsilon} = 10^{0}\ 1/\min$ and c) $\dot{\varepsilon} = 10^{1}\ 1/\min$.

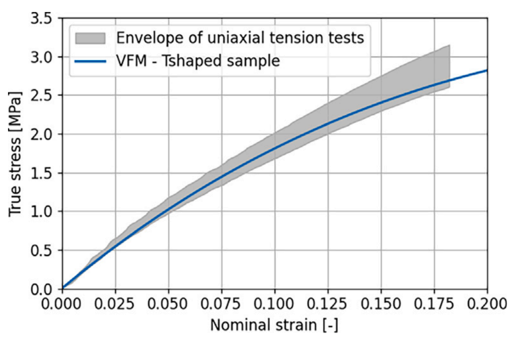


**Fig. 17.** Response of the Mooney-Rivlin material model with identified parameters under uniaxial loading and comparison with experimental results in uniaxial tension.

determined system of equations for unknown material parameters, a large overdetermined system of equations was derived from a large number of randomly generated kinematically admissible virtual displacement fields in order to reduce the influence of the choice of particular virtual fields on the outcome of the algorithm.

- A novel integration algorithm based on Voronoi tessellation was developed and implemented in order to properly deal with large deformations caused by the high compliance of the investigated material.

According to the obtained results one may conclude that:

- The use of the proposed VFM algorithm and developed experimental setup enables obtaining with just one sample results that are similar to those obtained as an average material response determined with a larger number of specimens.
- Observed discrepancies may be due to the use of a relatively simple hyperelastic material model. Alternative hyperelastic models such as those by Yeoh, Arruda–Boyce or Ogden might provide more accurate predictions.

Further research will be focused on implementing alternative hyperelastic models in the presented algorithm and validating them with the experimental results. While there is an increasing number of studies on the application and characteristics of flexible polyurethane adhesives, the identification of their material parameters in nonlinear constitutive laws is still not well investigated with just a few articles on this topic, e.g., [25,26]. The methods proposed in this article may emerge as a suitable tool for the description of such materials.

## CRediT authorship contribution statement

**Marcin Nowak:** Writing – original draft, Visualization, Validation, Software, Methodology, Investigation, Conceptualization. **Paweł Szeptyński:** Writing – original draft, Visualization, Validation, Methodology, Investigation, Conceptualization. **Sandra Musiał:** Writing – original draft, Visualization, Investigation, Conceptualization. **Klaudia Śliwa-Wieczorek:** Writing – original draft, Resources, Investigation, Conceptualization. **Michał Maj:** Supervision, Methodology, Investigation, Conceptualization.

## Declaration of competing interest

The authors declare that they have no known competing financial interests or personal relationships that could have appeared to influence the work reported in this paper.

## Acknowledgements

This research was funded in whole or in part by the National Science Centre, Poland under the OPUS call in the Weave programme, project No. 2021/43/I/ST8/00554.

## Data availability

The dataset supporting this study is publicly available on Zenodo: https://doi.org/10.5281/zenodo.18617429.

## References

[1] Pierron F, Grédiac M. The virtual fields method: extracting constitutive mechanical parameters from full-field deformation measurements. Springer New York; 2014. https://doi.org/10.1007/978-1-4614-1824-5
[2] ho Yoon S, Giannakopoulos I, Siviour CR. Application of the virtual fields method to the uniaxial behavior of rubbers at medium strain rates. Int J Solids Struct 2015;69–70 553–68. https://doi.org/10.1016/j.ijsolstr.2015.04.017
[3] Sutton MA, Orteu J-J, Schreier H. Image correlation for shape, motion and deformation measurements: basic concepts,theory and applications. 1st ed. Incorporated: Springer Publishing Company; 2009. https://doi.org/10.1007/978-0-387-78747-3
[4] Promma N, Raka B, Grédiac M, Toussaint E, Cam J-BL, Balandraud X, Hild F. Application of the virtual fields method to mechanical characterization of elastomeric materials. Int J Solids Struct 2009;46(3):698–715. https://doi.org/10.1016/j.ijsolstr.2008.09.025
[5] Jiang M, Dai J, Dong G, Wang Z. A comparative study of invariant-based hyperelastic models for silicone elastomers under biaxial deformation with the virtual fields method. J Mech Behav Biomed Mater 2022;136:105522. https://doi.org/10.1016/j.jmbbm.2022.105522
[6] Deng J, Guo X, Mei Y, Avril S. Fenics implementation of the virtual fields method (vfm) for nonhomogeneous hyperelastic identification. Adv Eng Softw 2023;175:103343. https://doi.org/10.1016/j.advengsoft.2022.103343
[7] van Huyssteen D, Reddy B. A virtual element method for isotropic hyperelasticity. Comput Methods Appl Mech Eng 2020;367:113134. https://doi.org/10.1016/j.cma.2020.113134
[8] Guélon T, Toussaint E, Cam J-BL, Promma N, Grédiac M. A new characterisation method for rubber. Polym Test 2009;28(7):715–23. https://doi.org/10.1016/j.polymertesting.2009.06.001
[9] He T, Liu L, Makeev A. Uncertainty analysis in composite material properties characterization using digital image correlation and finite element model updating. Compos Struct 2018;184:337–51. https://doi.org/10.1016/j.compstruct.2017.10.009
[10] Claire D, Hild F, Roux S. A finite element formulation to identify damage fields: the equilibrium gap method. Int J Numer Methods Eng 2004;61(2):189–208. https://doi.org/10.1002/nme.1057

[11] Nowak M, Szeptyński P, Musiał S, Maj M. Sub-global equilibrium method for identification of elastic parameters based on digital image correlation results. Arch Civ Mech Eng 2024;24(3):169. https://doi.org/10.1007/s43452-024-00979-6

[12] Meng S, Yousefi AAK, Avril S. Machine-learning-based virtual fields method: application to anisotropic hyperelasticity. Comput Methods Appl Mech Eng 2025;434:117580. https://doi.org/10.1016/j.cma.2024.117580

[13] Avril S, Grédiac M, Pierron F. Sensitivity of the virtual fields method to noisy data. Comput Mech 2004;4(7):439–52. https://doi.org/10.1007/s00466-004-0589-6

[14] Rahmani B, Villemure I, Levesque M. Regularized virtual fields method for mechanical properties identification of composite materials. Comput Methods Appl Mech Eng 2014;278:543–66. https://doi.org/10.1016/j.cma.2014.05.010

[15] Lourenço R, Georgieva P, Cueto E, Andrade-Campos A. An indirect training approach for implicit constitutive modelling using recurrent neural networks and the virtual fields method. Comput Methods Appl Mech Eng 2024;425:116961. https://doi.org/10.1016/j.cma.2024.116961

[16] Szeptyński P, Pochopień JG, Jasińska D, Kwiecień A. The influence of the flexibility of a polymeric adhesive layer on the mechanical response of a composite reinforced concrete slab and a reinforced concrete beam girder. Polymers 2024;16(3). https://doi.org/10.3390/polym16030444

[17] Kwiecień K, Kwiecień A, Stryszewska T, Szumera M, Dudek M. Durability of PS-polyurethane dedicated for composite strengthening applications in masonry and concrete structures. Polymers 2020;12(2830):1–16. https://doi.org/10.3390/polym12122830

[18] Rousakis T, Ilki A, Kwiecień A, Viskovic A, Gams M, Triller P, Ghiassi B, Benedetti A, Rakicevic Z, Colla C, Halici OF, Zajac B, Hojdys L, Krajewski P, Rizzo F, Vanian V, Sapalidis A, Papadouli E, Bogdanovic A. Deformable polyurethane joints and fibre grids for resilient seismic performance of reinforced concrete frames with orthoblock brick infill. Polymers 2020;12(2869):1–20. https://doi.org/10.3390/polym12122869

[19] Derkowski W, Kwiecień A, Zając B. CFRP strengthening of bent RC beams using stiff and flexible adhesives. Tech Trans Civ Eng 2013;6(1-CE):37–52. https://doi.org/10.4467/2353737XCT.14.003.1921

[20] Cruz JR, Seręga S, Sena-Cruz J, Pereira E, Kwiecień A, Zając B. Flexural behaviour of nsm CFRP laminate strip systems in concrete using stiff and flexible adhesives. Compos B 2020;195(108042):1–18. https://doi.org/10.1016/j.compositesb.2020.108042

[21] Śliwa Wieczorek K, Derkowski W, Binder E, Kwiecień A, Zając B, Halilovic E, Lotinac S. Shear stiffness and capacity of polyurethane flexible joint in timber-concrete composites. In: Proceedings of the fib symposium 2023 - building for the future: durable, sustainable, resilient, vol. 1; 2013. p. 476–85. https://doi.org/10.1007/978-3-031-32519-9_46

[22] Śliwa Wieczorek K, Scala AL, Derkowski W, Binder E. Longitudinal shear in timber–concrete composites with flexible adhesive connections—experimental and numerical investigations. Materials 2024;17(6055):1–26. https://doi.org/10.3390/ma17246055

[23] Nowak M, Maj M. Determination of coupled mechanical and thermal fields using 2D digital image correlation and infrared thermography: numerical procedures and results. Arch Civ Mech Eng 2018;18(2):630–44. https://doi.org/10.1016/j.acme.2017.10.005

[24] Ogden RW. Non-linear elastic deformations, Dover civil and mechanical engineering. Dover Publications; 1997.

[25] Pečnik JG, Gavrić I, Sebera V, Kržan M, Kwiecień A, Zając AB, Bogusław. Mechanical performance of timber connections made of thick flexible polyurethane adhesives. Eng Struct 2021;247(113125):1–12. https://doi.org/10.1016/j.engstruct.2021.113125

[26] Śliwa Wieczorek K, Zając B, Kozik T. Tests on the mechanical properties of polymers in the aspect of an attempt to determine the parameters of the mooney-rivlin hyperelastic model. Civ Environ Eng Rep 2020;30(2):1–14. https://doi.org/10.2478/ceer-2020-0016